Journal of Microscopy

Journal of Microscopy, Vol. 274, Issue 1 2019, pp. 32–44
Received 27 June 2018; accepted 24 January 2019

doi: 10.1111/jmi.12782

Estimation of filler macro-dispersion in rubber matrix by radiometric stereo microscopy

J. OHSER*, J. LACAYO-PINEDA†, M. PUTMAN‡, A. RACK§ & D. DOBROVOLSKIJ*,‖

*University of Applied Sciences, Darmstadt, Germany
†Continental Reifen Deutschland GmbH, Hannover, Germany
‡Nanotronics, 63 Flushing Avenue, Unit 241, Brooklyn, New York, USA
§European Synchrotron Radiation Facility, CS 40220, Grenoble, France
‖Fraunhofer ITWM, Fraunhofer-Platz 1, Kaiserslautern, Germany

Key words. Filler in rubber, Microtomography, Macro-dispersion, Radiometric stereo microscopy, Stereological estimation.

Summary

A new microscopic principle based on radiometric stereo microscopy is presented, which is designed for investigating macro-dispersion of filler in rubber. The image acquisition is combined with a stereological method of estimating the volume-weighted size distribution of the filler particles. Experimental results for carbon black filler in rubber obtained by radiometric stereo microscopy are compared with those from microtomography using synchrotron radiation, and, furthermore, a simulation study is used for evaluation. It turns out that using the new three-dimensional microscopic method, the size distribution of the filler particles can be estimated from fresh cuts of rubber with high accuracy, and thus it is an interesting alternative to well-established dark field microscopy.

Introduction

It is widely known that as an integral part of many imaging techniques, a wide range of image-processing algorithms is used. The probably most prominent example is computer tomography, where the tomographic reconstruction can be seen as an image-processing step. Much less accepted, however, is the fact that also image analysis is very closely tied to image acquisition. The reason for that might be that manufacturers of microscopes often focus on a widespread field of application with specific data analysis requirements. In the present article, we will give an example, namely measurement of macro-dispersion in rubber, in which acquisition, processing and analysis of images are closely interwoven. Furthermore, well-established but more expensive image acquisition techniques (in our case microtomography, μCT, with synchrotron radiation) and computer simulation are often applied to evaluate new and innovative techniques concerning their accuracy.

Macro-dispersion of globular filler particles (e.g. carbon black or silica) in a rubber matrix is an important quantity that depends on manufacturing parameters and influences various rubber properties. Therefore, it must be carefully adjusted during the incorporation process and investigated by industrial quality control. As pointed out in the industrial standard ASTM D7723–18 (2018), the macro-dispersion of filler particles is defined as the (volume-weighted) size distribution of the filler on a scale less than 100 μm but larger than 2 μm; see also ASTM D663–14 (2014) for dispersion of carbon black in rubber and ASTM D3053–17a (2017) for standard terminology used in rubber industry. Figures 1A to 1D outline the formation of nodges in a *fresh cut*. Quality control is usually based on freshly made planar sections (so-called fresh cuts) through rubber specimen, where a razor plate (or alternatively a discotom) is used for cutting. After stress retention of the rubber, one obtains no flat but rather a rough cutting surface in which the filler particles appear as imprints or bumps, called *nodges* in the industrial standard. These nodges can be made visible by classical light microscopy under dark field (DFM) illumination, e.g. the systems `disperGRADER+` from TECHPRO or the `disperGRADER Alpha View` from Alpha Technologies, which were specifically designed for rubber (and plastics) inspection. However, it has proved to be very difficult estimating the size distribution of the filler particles from the observed white spots in dark field images, because the size of the white spots strongly depends on imaging parameters as well as the threshold to be chosen for binarization of the dark field images. Even if an appropriate threshold could be chosen based on an objective criterion, e.g. Otsu's threshold Otsu (1979), that would allow to segment the section profiles and to measure their sizes accurately, it would still be necessary to compute

*Equally contributing authors.

Correspondence to: Dascha Dobrovolskij, Fraunhofer ITWM, Fraunhofer-Platz 1, 67663 Kaiserslautern, Germany; email: dascha.dobrovolskij@itwm.fraunhofer.de

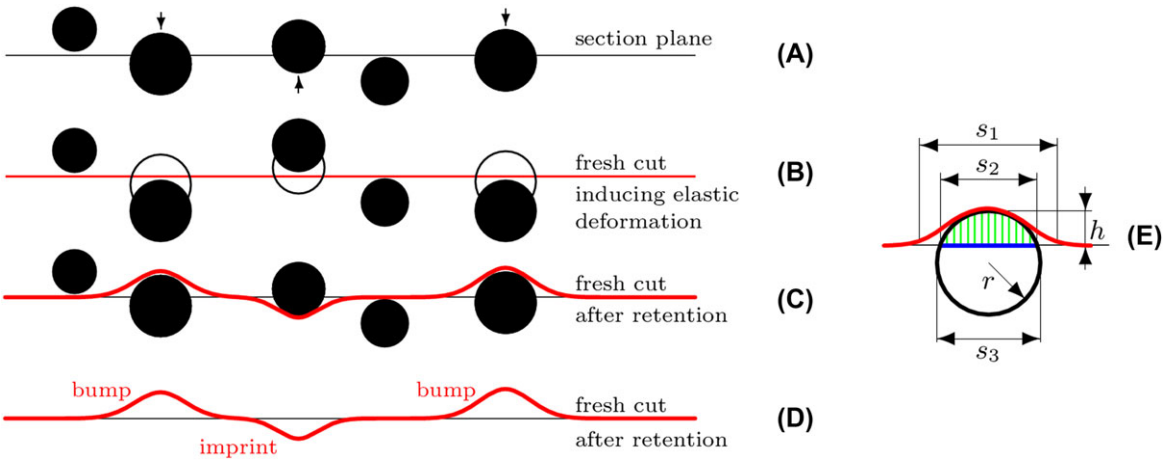

Fig. 1. Scheme of forming nodges after retention in a freshly made cut: (A) filler particles close to the section plane before cutting the rubber, where the arrows mark the particle shift during cutting, (B) shifted particles induce elastic deformation of the rubber matrix, (C) the particle positions after retention of the rubber matrix, (D) the nodges (imprints and bumps) in the fresh cut and (E) a sphere of diameter $s_3 = 2r$, a sphere cap (green) and its height h, the size s_1 of a bright spot from a bump, the size s_2 of the section profile (blue).

the size distribution of the filler particles from an estimated size distribution of the section profiles, e.g. by solving Wicksell's corpuscle problem; see Wicksell (1925). The latter is numerically instable, i. e. small errors of the estimated size distribution of the section profiles lead to large errors of the computed filler size distribution (Ohser & Sandau, 2000). Applying DFM combined with filler dispersion estimation as described in ASTM D7723–18 (2018) appears to be a fingerprint method only. For this reason, the new microscope `nSPEC 3D` from Nanotronics, New York, was applied for rubber inspection. The principle used for surface imaging is based on radiometric stereo (also known as *photometric stereo* or *shape from shading*) allowing for perfect three-dimensional reconstruction of curved surfaces of fresh cuts (Woodham, 1980; Zhang *et al.*, 1999). From this reconstruction, it is possible to estimate the depth of particle imprints, respectively, the height of bumps (in the following referenced as *height of nodges*) as well as their volumes.

The stereological problem to be solved is the estimation of the size distribution of the globular filler particles in rubber from samples of the height and volume of nodges, where the shape of the particles is assumed to be spherical. The problem is similar to Wicksells corpuscle problem, where the diameter distribution of a macroscopically homogeneous system of spheres embedded in an opaque matrix is estimated from the diameter distribution of section circles observed in a planar section through the specimen (Wicksell, 1925, 1926). We present a new stereological formula, which relates the size distribution of the filler particles to the volume-weighted height distribution of the nodges. The corresponding integral equation is solved numerically, where methods published, e.g. in Ohser & Mücklich (2000) and Chiu *et al.* (2013) are adapted to the specific problem. The accuracy of the method is evaluated by a simulation of nodge formation during the cutting process based on an assumption made for the filler particle distribution. Furthermore, the filler particle distribution stereologically estimated from the height and volume of nodges observed by radiometric stereo is compared with that estimated from three-dimensional (3D) images obtained by μCT using synchrotron radiation.

Materials and methods

The critical influence of filler dispersion on rubber quality has been a broad area of study for nearly 70 years, where we remark that in industrial quality control the dispersion of filler was usually not measured directly. Instead, materials testing methods were applied to conclude on the compounding energy of the rubber, which in turns is influenced by the filler dispersion. Hess & Chrico (1977) gives a good introduction to carbon black dispersion and describes various methods to characterize dispersion. These methods can broadly be put into three categories: electrical methods, mechanical methods and optical/microscopic methods. Optical methods have become common as direct, rather than cumulative measurement for dispersion; see also Wang (2005) and Le *et al.* (2008).

Until now, DFM has been established as the standard two-dimensional (2D) image acquisition method for detecting filler particles in fresh cuts, but it is limited by several factors, most relevant being that a single light vector is used (or multiple vectors simultaneously). Frequently, this can lead to pixels being covered by shadows. For this reason, the 3D topology of the surface cannot be reconstructed from conventional dark field images.

In the standard ASTM D7723–18 (2018), the calculation of macro-dispersion in a rubber matrix is regulated. In terms of this standard macro-dispersion is the size distribution of filler

particles with size at least 2 μm. Because of the large number of small filler particles, the representation of the size distribution as the classical number-weighted size distribution does not make sense. Instead, we will use the volume-weighted size distribution below. This is analogous to the estimation of the area-weighted size distribution of the white spots in dark field images. Furthermore, in ASTM D7723–18 (2018) the so-called degree of dispersion defined as $1 - \mathrm{URF}/L$, where URF denotes the area fraction of the unresolved filler (and URF is usually estimated from DFM images as the area fraction of the white spots of size at least 2 μm), L is filler volume fraction in the compound (which is a technological parameter of the filler reinforcement process), and the degree of dispersion is usually given in per cent. The volume fraction L is estimated from the filler mass, the filler density, the compound mass and the compound density. If these data are unknown, L is set to its technological maximum, $L = 35\%$. Basically, the area fraction of the section profiles of the unresolved filler is equivalent to its volume fraction, but there are two problems: The first one is the arbitrary choice of the lower limit of the particle size for the macro-dispersion. In the industrial standard, it is forced as 2 μm, but in most 2D inspection systems this limit is set for the size of the particle section profiles (s_2 in Fig. 1E), not for the size s_3 of the particles themselves, where we remark that even large particles can have small section profiles. The second problem is that there is only a weak relationship between the size of the bright spots (s_1 in Fig. 1E) in DFM images (resulting from the bumps in the fresh cuts) and true size s_2 of the section profiles. In most cases, bright spots appear much larger than the corresponding section profiles. Furthermore, imprints are hard to see in dark field images and, as a consequence, they might be undetectable. These disadvantages of DFM can be overcome, e.g. by radiometric stereo microscopy (RSM) or μCT using synchrotron radiation, where RSM can be applied in laboratories for industrial quality control and μCT is recommended for validating measurements.

Imaging of nodges using radiometric stereo

Radiometric stereo images can be obtained from a single CCD camera under subsequent illumination from six constant lighting vectors at identical angles of incidence of 45° in relation to the optical axis, where the azimuthal distance between the lighting vectors is 60°. Here, we use the camera type Allied Vision Prosilica GT 2750, a sensor Sony ICX694 with a maximum frame rate of 19.8 fs^{-1}. A Nanotronics system `nSPEC 3D` applies a standard 20× Olympus objective with a numerical aperture (NA) of 0.40 and a working distance of 12 mm (see Fig. 2). The system uses broad spectrum white light microscopy with LEDs (Prizmatix Ultra High LED White Light) as an illumination source. An illumination mode along a modified dark field channel has been constructed, where an oblique and opaque disk is rotated according to pre-defined algorithmic instructions to various locations on this channel,

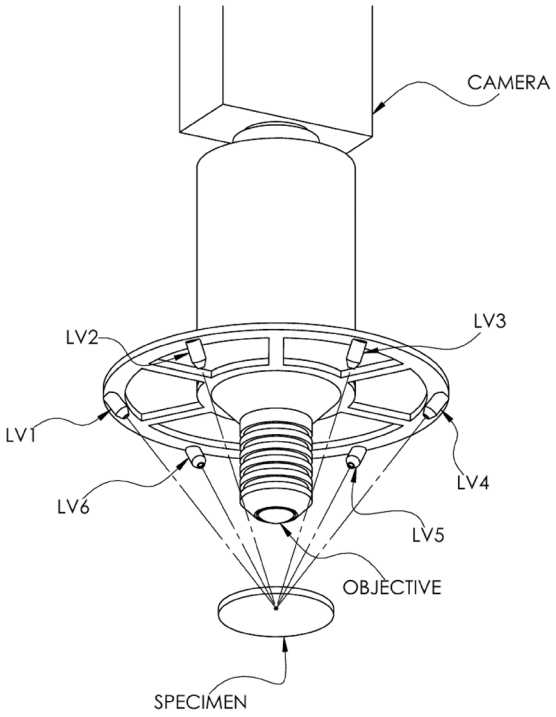

Fig. 2. Scheme of the microscope `nSPEC 3D` with the six light vectors `LV1`, . . . ,`LV6` representing the positions of the LEDs relative to the focal point of the objective. The angle between the light vectors and the optical axis is 45°, and the azimuthal distance between them is 60 degrees.

suppressing illumination from the complete dark field channel by blocking all but a single lighting vector. The six 2D images are acquired by the camera with 2750×2200 pixels. The adjusted pixel size at 20× is 0.227 μm.

The captured 2D images are processed further by some preprocessing steps that include sequentially improved exposure. The latter is based on a pre-sampling out of a separate database consisting of the 1500 images taken by radiometric stereo from carefully selected samples. The improved exposure is set, and the individual illumination vectors are adjusted to have consistent lighting for future scans. In this way, the system improves with time (from one reconstructed topography to the next) when various fields of view of the sample or samples of the same type are investigated. By using the multiple vector lighting system combined with this kind of auto exposure settings, one obtains six pre-processed 2D images as the input for topography reconstruction of the fresh cut.

In the `nSPEC 3D`, the reconstruction of topography by radiometric stereo from the six pre-processed 2D images relies on calculation of surface normals using Lambert's equation (Woodham, 1974, 1980; Ray *et al.*, 1983; Zhang *et al.*, 1999); see also Miché *et al.* (2005) and Arecchi *et al.* (2007), where the normals of the curved surface are calculated from the lighting vectors `LV1`, . . . ,`LV6` and the measured intensities represented by the pixel values of the 2D images. The core is the solution of

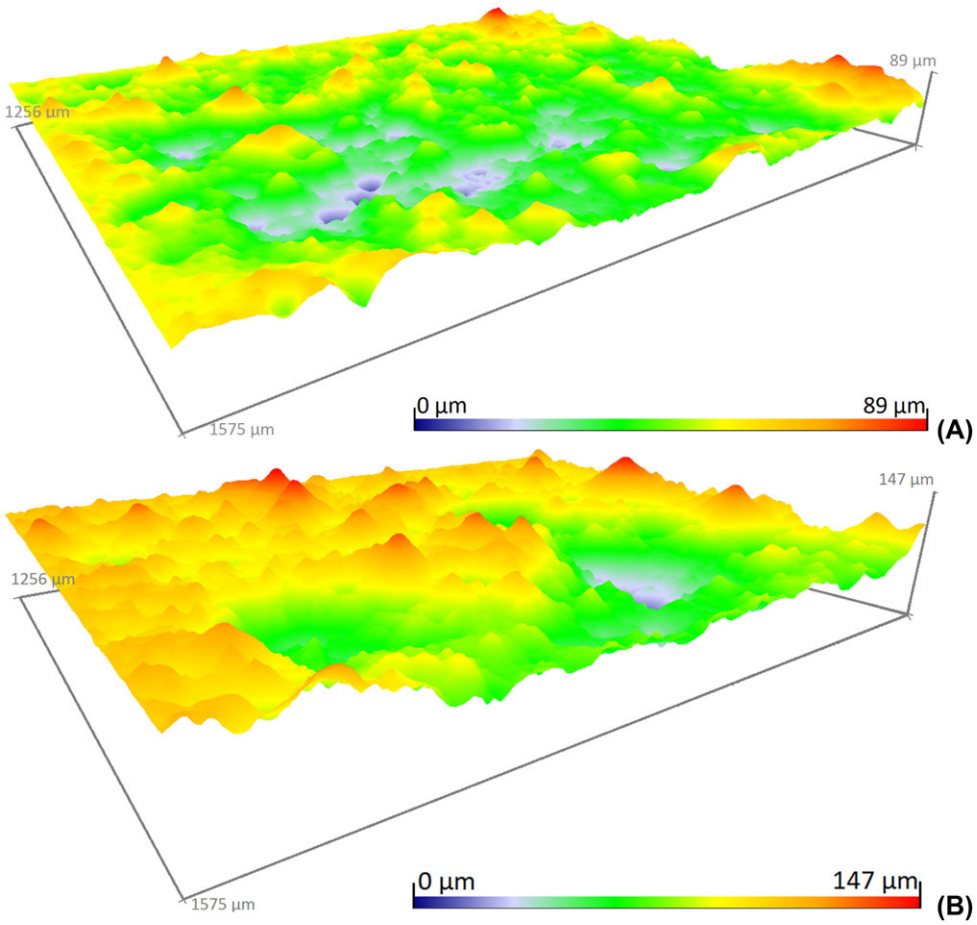

Fig. 3. Visualizations of the reconstructed surface of fresh cuts of rubber with low degree of dispersion. The images were taken by radiometric stereo using the microscope `nSPEC 3D` with a 20×/0.40NA: In both images, the curved surface is encoded as the height depending on the pixel position, 825×660 pixels of size 1.91 µm. The resolution on the *z*-direction is about 1.0 µm.

a linear equation system (which of course is overdetermined for six lighting vectors and therefore usually solved by singular value decomposition). As a pre-condition of the applicability of this technique, it is assumed that a sample is Lambertian in nature; however, sometimes spectral distortion are observed on samples that are not purely Lambertian (Frankot & Chellappa, 1990). In the simplest case, these distortions can be detected by simple thresholding the reconstructed topography, where values at least a given threshold level are ignored, because they cannot come from a sufficiently smooth Lambertian surface. The resulting gaps in the reconstructed topography are filled by the mean pixel value of the nearest four neighbouring pixels. In the optical setup of the `nSPEC 3D`, each of the lighting vectors illuminates only a partial field of view; therefore, only those with varying in pixel values in the obtained image are used for calculating the normals. Any light that does extent beyond the field of view, due to ambient light, or surface shape, is not recorded on the imaging sensor. Fig. 3 shows examples of the reconstructed topography of fresh cuts of rubber infiltrated with carbon black.

Finally, a reflectance mapping can be derived from the reconstructed topography, whose information could in turn be used for future reconstruction of the topography of further field of views of the same sample or of other samples. Therefore, not only the exposure is sequentially improved but also database for the improvement of the exposure (used in the pre-processing step) can be updated with each reconstruction. This is an important aspect of our approach and has provided good results for surfaces with Lambertian quasi-specular reflectance. A challenge has traditionally been to provide this information in the presence of non-uniform albedo. Radiometric stereo observed here shows no such effect.

The frame rate of RSM in the present setting is about $0.35\,\mathrm{fs}^{-1}$. This involves the capturing of the six 2D images (corresponding to the six light direction vectors `LV1, ...,LV6`), the pre-processing of the images, the reconstruction of the 3D topography and the updating of the database. As a consequence, the RSM is more time consuming than DFM. Nevertheless, this frame rate of RSM should be sufficient for many applications in industrial quality control.

Radiometric stereo has several key advantages over other techniques such as microscopy based on focal stacking, also known as *shape from focus* or *depth from defocus* (DFD). Focal stacking uses the bright-field channel of an optical microscope with an objective of high numerical aperture and captures a sequence of 2D images at different focal depths, where in each of these images different parts of the specimens topography are in focus. Roughly speaking, the core of DFD is the detection of the in-focus regions of each image. Then the height of the topography at a position is estimated from the index of that 2D image, which is in-focus at this position. More precisely, the height is estimated as the product of the index and the focal stacking step width; see, e.g. Chen *et al.* (2008) and Clark & Brown (2015) for more details and advanced techniques. Two aspects of defining shape and z-height are problematic. Most notable is the inability to define the top focus plane due to the likelihood of the final step size over or under shooting the top of the feature. Furthermore, by DFD the reconstruction of those surface elements of the topography is faulty, for which the surface normal is approximately perpendicular to the optical axis. In RSM, this problem usually does not occur because the directions of illumination considerably differ from that of the detection.

Microtomography of filler in rubber

Tomographic data sets were acquired at beamline ID19 of the European Synchrotron Radiation Facility (ESRF) in Grenoble, France (Weitkamp *et al.*, 2010). In order to limit potential dose issues to the sample while maintaining sufficient contrast, a photon energy of 35 keV was chosen. In order to reach sufficient photon flux density in combination with a narrow bandwidth illumination, the beamline's double-multilayer monochromator was used to select the corresponding harmonics from two undulators (type: u32). Additionally, 16 so-called compound-refractive lenses where inserted into the X-ray optical beampath as collimators in order to further increase the photon flux density at the position of the sample. A mild diffuser upstream of the sample was used to reduce wave front modulations due to the multilayer reflection (Rack *et al.*, 2010). An indirect X-ray image detector was applied in order to obtain highly resolved radiographic projection images of the sample: a $10\times/0.3$NA microscope objective projects the luminescence image of a single-crystal scintillator via a tube lens onto the sCMOS-based sensor of a camera (type: pco.edge 5.5, PCO AG, Germany). The effective pixel size of the imaging system was 0.64 μm (Douissard *et al.*, 2012). In order to enhance the contrast, so-called propagation-based phase contrast was used. Here, by leaving a drift space between sample and detector (40 mm in our case) the refraction at interfaces results in an edge enhancement; see Cloetens *et al.* (1996). To guaranty good tomographic reconstruction with a sufficient signal-to-noise ratio, 3600 projection images were acquired over a 180° scan. For the reconstruction by means of filtered back-projection in combination with phase-retrieval using Paganin's approach, the in-house developed software PyHST_2 was used (Paganin *et al.*, 2002; Weitkamp *et al.*, 2011; Mirone *et al.*, 2014). The high contrast in the images between the filler particles and the rubber matrix enables further image processing and analysis.

The use of partially coherent X-rays easily available at a synchrotron light source is highly beneficial for contrast, especially for weakly attenuating samples. Frequently, when laboratory-based X-ray sources are used, the contrast within the images is roughly given by the local physical mass density. Hence, materials with similar densities like in the present case are poorly contrasted. The use of (partially) coherent illumination in combination with phase-retrieval techniques allows for exploiting the full (complex-valued) refractive index of the materials. The application of phase-retrieval techniques allows one to establish a direct correlation between a voxel, its grey-value and the corresponding material phase it represents. The resulting contrast is an order of magnitude more sensitive to material changes than the plain attenuation signal.

Estimation of particle size distribution

Now, we present an approach to estimate the size of filler particles based on the fresh cuts. First, the RSM images require some image processing steps. The additive shading in images of fresh cuts obtained by radiometric stereo can be removed by generating a reference image using alternate filtering, i.e. morphological opening followed by closure (see, e.g. Angulo, 2011) with adapted structuring elements. The reference image is subtracted from the original one. The nodges in the image difference are segmented by watershed transform (Beucher & Meyer, 1993), where the local minima and maxima of the surface of the fresh cut serve as markers, and oversegmentation can be suppressed by a so-called h-min-transform (Soille, 1999).

The stereological problem consists of estimating the size distribution of the filler particles in the rubber matrix from observations of height and volume of nodges in freshly made cuts. This problem can only be solved if information about the particle shape is available. To make the problem feasible, we will assume in the following that the filler particles are of spherical shape, where the half mean particle size (i.e. the mean width over all space directions) serves as an estimate of radius of the adapted sphere. The sphere assumption is justified by two facts: First, from tomographic investigations we know that carbon black consists of globular particles of approximately spherical shape; see Section **Tomography**. Second, the macro-dispersion of the filler is characterized by the volume-weighted particle size distribution instead of the classical number-weighted size distribution, and even estimates of volume-weighted distributions are robust with respect to deviations from spherical shape, i.e. small deviations from spherical particle shape induce only a small bias of the

stereologically estimated volume-weighted size distribution; see Ohser & Mücklich (2000), Chapters 6 and 7.

Stereological equation

Let r be the radius of a spherical filler particle inducing a nodge in the fresh cut. Instead of nodge height and volume, we consider the height h and volume v of the sphere cap cut off by the section plane (see Fig. 1E). A simple geometric consideration yields the relationship

$$v(r,h) = \begin{cases} \frac{\pi}{3}h^2(3r-h), & h \le r \\ 0, & \text{otherwise} \end{cases},$$

which makes clear that the radius r of an individual particle could be obtained from the height h and the volume v. However, one should take into account that h and v differ from the observed height respectively, volume of the nodges. That is why we are choosing a stochastic approach and estimate the particle size distribution from the height distribution of nodges.

First, we introduce the filler particle density N_V (i.e. the mean number of filler particles per unit volume of the rubber specimen) and the nodge density N_A (the mean number of nodges per unit area of the fresh cut) which are related to each other by $N_A = 2N_V\bar{r}$, where $\bar{r}$ is the mean particle radius. Assume now that the sphere radius distribution has a probability density function $f(r)$ and the third moment exists, then

$$f_V(r) = \frac{4\pi}{3\bar{v}}r^3 f(r)$$

is the probability density function of the volume-weighted radius distribution, which serves as a quantity characterizing the degree of dispersion. Here, the mean particle volume

$$\bar{v} = \frac{4\pi}{3}\int_0^\infty r^3 f(r)dr$$

is used as a normalization constant. The corresponding probability distribution function $F_V(r) = \int_0^r f_V(s)\,ds$ for $r \ge 0$ can be interpreted as follows: The expression $N_V(1 - F(r))$ is the mean number of spheres per unit volume with radii at least r, and $V_V\big(1 - F_V(r)\big)$ is the volume fraction of spheres with radii at least r. Furthermore, let $G_V(h)$ be the probability distribution function of the volume-weighted height distribution of the sphere caps, i.e. $V_A\big(1 - G_V(h)\big)$ is the total volume of all nodges per unit area of the fresh cut with heights at least h, where V_A is the total volume of all sphere cups per unit are of the fresh cut.

The corresponding probability density function $g_V(h)$, as far as it exists, is related to $f_V(r)$ by the integral equation

$$\begin{aligned} g_V(h) &= \frac{1}{c}\int_0^\infty v(r,h)\,f(r)\,dr \\ &= \frac{3\bar{v}}{4\pi c}\int_h^\infty \frac{h^2}{r^3}(3r-h)\,f_V(r)\,dr, \qquad h \ge 0, \quad (1) \end{aligned}$$

where c is again a normalization constant (chosen such that $g_V(h)$ forms a probability density function). The kernel of the integral on the right-hand side of Eq. (1) is (up to a multiplication constant) the function $v(r,h)/\frac{2\pi}{3}r^3$, which can be interpreted as the (conditional) probability that the volume of a sphere cup of random height is less than the volume of a sphere cup of height h, given that the (random) sphere radius is r and the sphere hits the fresh cut. As a consequence, Eq. (1) is a special case of the Volterra equations considered in Ohser & Nagel (1988), where a mathematical proof is given; see also Ohser & Sandau (2000) for a review on inverse problems of estimating particle size distributions.

Gamma distributed radii. To give an impression of how Eq. (1) works, we compute the probability density function $g_V(h)$ of the volume-weighted height distribution of the sphere caps for given probability density function $f_V(r)$ of the volume-weighted radius distribution. One gets explicit formulas, e.g. for the very rich class of gamma distributed particle radii with the distribution parameters $\lambda > 0$ and $\alpha > 0$. From

$$f(r) = \frac{\lambda^\alpha r^{\alpha-1}}{\Gamma(\alpha)}\,e^{-\lambda r}, \qquad r \ge 0$$

with Euler's gamma function $\Gamma(z) = \int_0^\infty t^{z-1}\mathrm{e}^{-t}\,dt$ it follows from integration by parts

$$f_V(r) = \frac{\lambda^{3+\alpha} r^{2+\alpha}}{\Gamma(3+\alpha)}\,e^{-\lambda r}, \qquad r \ge 0,$$

which is again the probability density function of a gamma distribution with the parameter $\alpha + 3$. Now, putting $f_V(r)$ in Eq. (1) yields

$$g_V(h) = \frac{4h^2\lambda^3\big(3\Gamma(1+\alpha,\lambda h) - \lambda h\Gamma(\alpha,\lambda h)\big)}{3\Gamma(4+\alpha)}, \qquad h \ge 0,$$

where the recursion formula $\Gamma(1+z,u) = u\Gamma(z,u) + u^z\mathrm{e}^{-u}$ was exploited for the upper incomplete gamma function $\Gamma(z,u) = \int_u^\infty t^{z-1}\mathrm{e}^{-t}\,dt$. The mean radius is $\bar{r} = \alpha/\lambda$, and the volume-weighted mean is $\bar{r}_V = (\alpha+3)/\lambda$.

In the following, we will make use of the fact that for $\alpha = 1$ the gamma distribution simply forms an exponential distribution, and for $\alpha = \frac{n}{2}$ and $\lambda = \frac{1}{2}$ the gamma distribution is equivalent to a chi-square distribution.

Exponentially distributed radii. For the density function $f(r) = \lambda\,e^{-\lambda r}$, $r \ge 0$, we have

$$f_V(r) = \frac{\lambda^4 r^3}{6}\,e^{-\lambda r}, \quad r \ge 0 \qquad \text{and}$$

$$g_V(h) = \frac{\lambda^3 h^2}{18}(3 + 2\lambda h)\,e^{-\lambda h}, \quad h \ge 0.$$

The functions $f_V(r)$ and $g_V(h)$ are depicted in Fig. 4A for $\lambda = 0.4$. For exponentially distributed radii, the difference of both functions is very small and, as a consequence, an estimate

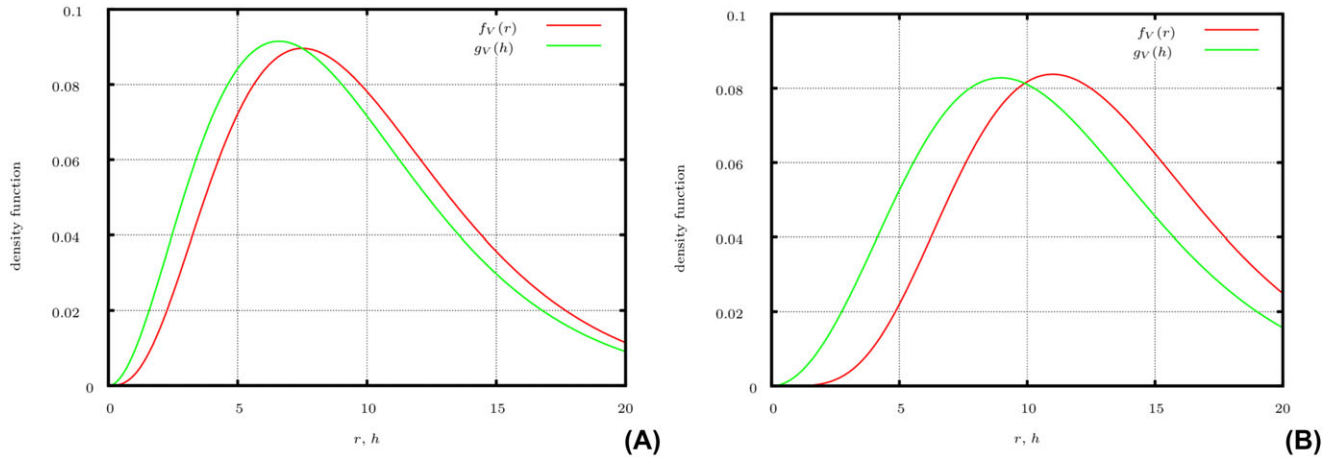

Fig. 4. The probability density functions $f_V(r)$ and $g_V(h)$ for (A) exponentially distributed radii with $\lambda = 0.4$ and (B) for chi-square distributed radii with $n = 7$.

of $g_V(r)$ could be used in this case as an estimate of the macro-dispersion $f_V(r)$.

Chi-square distributed radii. For χ^2_n-distributed radii with the probability density function

$$f(r) = \frac{r^{\frac{n}{2}-1}}{2^{\frac{n}{2}}\Gamma\left(\frac{n}{2}\right)} e^{-\frac{r}{2}}, \qquad r \geq 0$$

it is

$$f_V(r) = \frac{r^{2+\frac{n}{2}}}{2^{3+\frac{n}{2}}\Gamma\left(3+\frac{n}{2}\right)} e^{-\frac{r}{2}}, \qquad r \geq 0$$

and

$$g_V(h) = \frac{h^2\left(6\Gamma\left(1+\frac{n}{2}, \frac{h}{2}\right) - h\Gamma\left(\frac{n}{2}, \frac{h}{2}\right)\right)}{12\Gamma\left(4+\frac{n}{2}\right)}, \qquad h \geq 0.$$

It is easy to see that $f_V(r)$ is the probability density function of the chi-square distribution with the parameter $n+6$. A comparison of both functions for higher order n shows that they can considerably differ (see Fig. 4B). This shows that in general an estimate $g_V(r)$ cannot serve as a suitable estimate for the macro-dispersion $f_V(r)$.

Stereological estimation

The above explanation might suggest that the height distribution of the nodges is to be evaluated from the size distribution of the filler particles. Of course, that is not the case. Instead, from the height distribution of the nodges, which can be determined at a fresh cut, we have to estimate the particle size distribution. This means that we have to solve an inverse problem, where the integral equation (1) must be solved for the unknown macro-dispersion $f_V(r)$. For this purpose, we turn form the probability density functions $f_V(r)$ and $g_V(h)$ to the corresponding probability distribution functions $F_V(r)$ and $G_V(h)$, respectively. Integration of Eq. (1) yields

$$\begin{aligned} G_V(h) &= \int_0^h g_V(t)\,dt = c\int_0^h \int_0^\infty v(r,t) f(r)\,dr\,dt \\ &= \frac{3\bar{v}}{4\pi c}\int_h^\infty \frac{h^3}{r^3}\left(r - \frac{h}{4}\right) F_V(dr), \qquad h \geq 0 \quad (2) \end{aligned}$$

which is a Volterra integral equation. This equation can be solved as follows: Let Δ be the width of the bins for the height h of the nodges as well as for the radius of the particles. Furthermore, let be chosen a bin number m such that $m\Delta$ is largest height occurring in the sample. Then numerical integration of the right-hand side of Eq. (2) by simple rectangular quadrature rule gives the linear equation system

$$\begin{aligned} G_V(k\Delta) &= \frac{3\bar{v}}{4\pi c}\int_h^\infty \frac{(k\Delta)^3}{r^3}\left(r - \frac{k\Delta}{4}\right) F_V(dr) \\ &\approx \frac{3\bar{v}\Delta}{4\pi c}\sum_{i=k}^{m} \frac{k}{i}\left(i - \frac{k}{4}\right)\left(F_V(i\Delta) - F_V((i-1)\Delta)\right), \\ &\quad k = 1, \ldots, m. \end{aligned}$$

Finally, introducing the vectors $\varphi = (\varphi_i)$ and $\vartheta = (\vartheta_k)$ of the relative frequencies (histograms) $\varphi_i = F_V(i\Delta) - F_V((i-1)\Delta)$ for $i = 1, \ldots, m$ respectively, $\vartheta_k = G_V(k\Delta) - G_V((k-1)\Delta)$ for $k = 1, \ldots, m$, the last equation can be rewritten as

$$\vartheta \approx \frac{3\bar{v}\Delta}{4\pi c} P\varphi \qquad (3)$$

with the upper triangular matrix $P = (p_{ki})$ of coefficients

$$p_{ki} = \frac{k^3}{i^3}\left(i - \frac{k}{4}\right) - \frac{(k-1)^3}{i^3}\left(i - \frac{k-1}{4}\right)$$

for $k = 1, \ldots, m$, $i = k, \ldots, m$ and $p_{ki} = 0$ for $i < k$. The transition matrix P is regular, i.e. its inverse P^{-1} exists, and

thus the unknown vector φ of the frequencies of the volume-weighted particle size distribution can be obtained from the vector ϑ of the frequencies of the volume-weighted height of nodges by

$$\varphi \approx \frac{4\pi c}{3\bar{v}\Delta} P^{-1}\vartheta, \tag{4}$$

where the vector ϑ is replaced by an estimate obtained from a sample of height and volume of nodges observed in the fresh cut, e.g. by radiometric stereo.

Examples of estimating the histogram φ of the filler particle size distribution from the histogram ϑ of the nodge height distribution estimated using Eq. (4) are shown in Fig. 5 where images taken by RSM. Fig. 5A is for a rubber (R1) in an early state of carbon black filler incorporation and in Fig. 5B is for a rubber (R2) with advanced incorporated carbon black. As one can see, the estimate ϑ can be considerably different from φ as in Fig. 5A, but it is also possible that ϑ is close to φ as in Fig. 5B. The root-mean-square deviation between the ϑ_k and the $\varphi_k(\text{est})$ given by

$$\sqrt{\frac{1}{m}\sum_{k=1}^{m}\left(\vartheta_k - \varphi_k(\text{est})\right)^2}$$

is 4.1% for the rubber specimen R1 and 0.8% for R2, respectively. Notice that the condition number of the transition matrix P is small and, as a consequence, small errors of estimating ϑ usually induce only small errors of the expression on the right-hand side of Eq. (4). For example, for $m = 12$ the condition number with respect to the spectral norm is $\text{cond}\, P = 1.141$. For comparison, under similar conditions the condition number of the transition matrix for the numerical solution of Wicksell's corpuscle problem is 8.28, i.e. solving Wicksell's problem is much more numerically instable.

The total time for processing the RSM images, including the segmentation of the nodges and measuring their height and volume, is about 0.5 s. It depends slightly on the nodge number. The core of the solution of the stereological problem given by Eq. (4) is the computation of the inverse of the matrix P which is done for a usual bin number $12 \leq m \leq 20$ in nanoseconds.

Evaluation

The stereological method presented in the previous section is now evaluated in a twofold way: First, a simulation study is made, where the nodges in a fresh cut are generated by simulating the shift of the filler particles during virtual cutting and the deformation field after retention is computed by finite element method. This allows a comparison of the stereologically estimated filler size distribution with the true one used as input of the simulation. Second, the estimated filler size distribution is compared with that one obtained by segmenting the filler particles in μCT images of the rubber microstructure.

A direct comparison of results from RSM and DFM is not possible, because RSM generates 3D images of the curved surface of fresh cuts while DFM images are 2D, and from these 2D images one can estimate only the lateral extent of the nodges. The two quantities, namely the size distribution of the particles and the distribution of the lateral size of the nodges, are not comparable. It can be concluded, however, from the distribution of the lateral nodge size (s_1 in Fig. 1E) on the distribution of the particle size s_3, where we remark that in case of Rayleigh-distributed particle sizes both distributions are identical; see Ohser & Mücklich (2000). (The latter, in turns, is only fulfilled if the size s_1 of the nodges in fresh cuts is identical with the size s_2 of the particle section profiles in the corresponding planar section, which is generally not the case.) But one can also give examples in which both distributions differ: For example, if all particles are of the same size, then the mean lateral size of the nodges is $\pi/4$ times smaller than the particle size. If, on the other hand, the particle size is χ^2_n-distributed with $n \geq 6$, then the mean lateral size of the nodges is larger than the mean particle size. In other words, whether measurements made on RSM and DFM images match or not depends on the particle size distribution itself, but that is just the quantity we want. Furthermore, we state that the stereological estimation of the particle size distribution from samples of lateral nodge sizes (obtained from DFM images) by solving Wicksell's corpuscle problem is numerically more unstable than estimating the particle size distribution from samples of height and volume of nodges (obtained from RSM images). This follows immediately from comparison of the condition numbers for the transition matrices P; see Section **Stereological Equation**. Finally, measurements of the lateral nodge size s_1 made on DFM images can considerably differ from the size s_2 of the section profiles; see Fig. 1E. This difference, which depends on the contrast of DFM images as well as on the choice of the threshold level for binarization, can lead to an considerable bias of the estimated particle size distribution.

Simulation study

We start from a spatial system of spheres whose centres form a Poisson point field, i.e. the number of spheres in the specimen is Poisson distributed and the centres are uniformly distributed in the specimen. Furthermore, the random radii are stochastically independent of each other and exponentially distributed with $\lambda = 1\ \mu\text{m}^{-1}$ (i.e. $\bar{r}_V = 4\ \mu\text{m}$). The use of the Poisson point field is motivated by the fact that the small number of particles per unit area and the small particle size imply that overlapping is rare and, thus, affects the results of the simulation only slightly. The filler particles are assumed to be inelastic, and for the uniform Young's modulus and the uniform Poisson's ratio of the rubber matrix we are setting $E = 0.1$ GPa and $\gamma = 0.5$, respectively. In the initial state, the stress field is assumed to be zero almost everywhere. For a chosen section plane with a normal direction parallel to the z-axis, all spheres hitting this

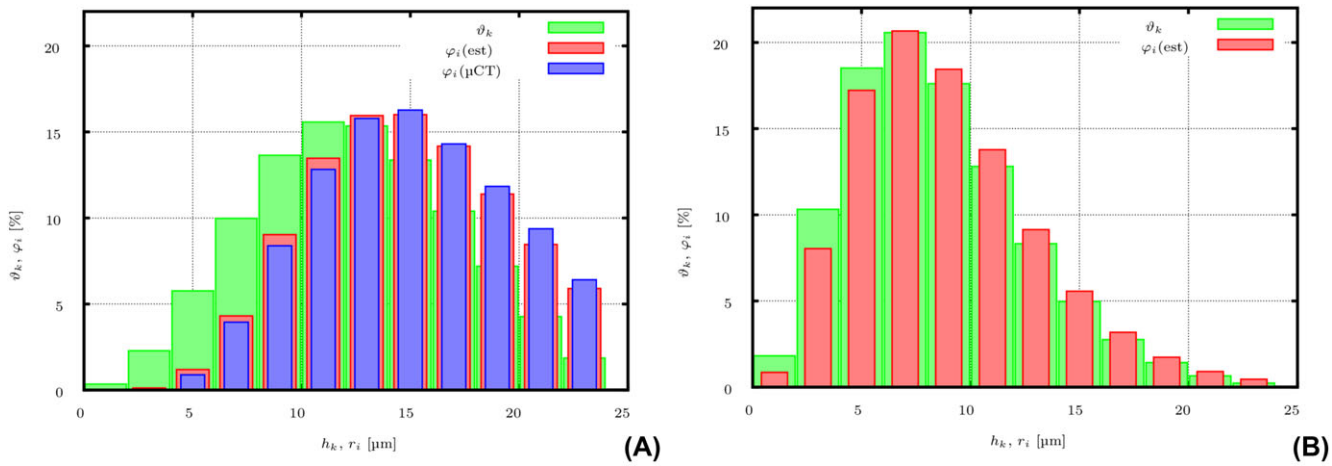

Fig. 5. Histograms ϑ and φ of volume-weighted distributions of nodge height respectively, filler particle size, bin width of 2 µm: (A) rubber R1 with an early state of filler incorporation, data from 217 nodges; (B) rubber R2 with an advanced incorporation, data from 276 nodges.

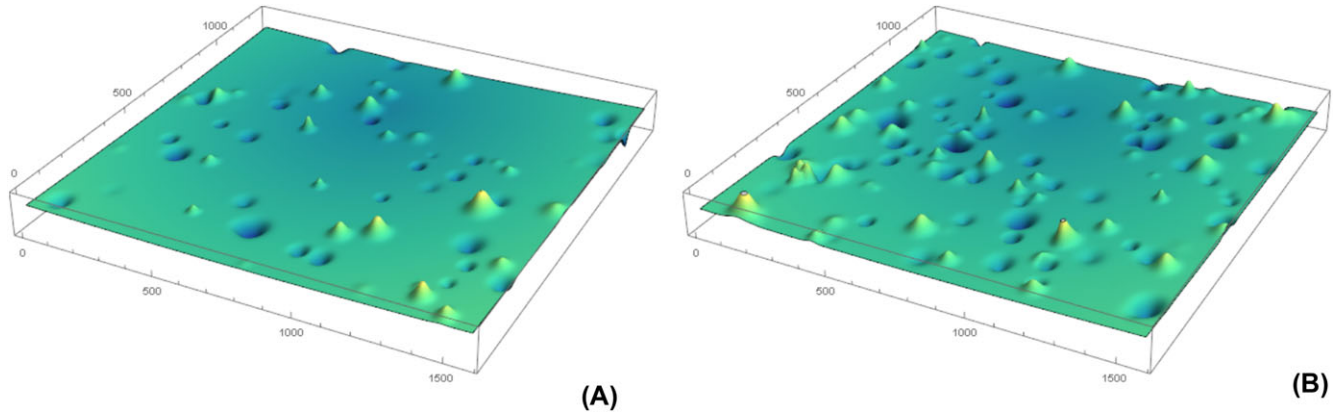

Fig. 6. Visualization of nodge patterns in fresh cuts simulated by numerical computation of the deformation of a rubber specimen after virtual cutting a rubber specimen with a razor plate: (A) a low and (B) a higher number of spherical filler particles per unit volume of the specimen.

plane are shifted perpendicular to this plane as long as they are only touching the plane; see Fig. 4B. These shifts induce a stress field in the rubber matrix (Bathe, 1996; Zienkiewicz *et al.*, 2005); see also Chapter 9 in Ohser & Schladitz (2009). Now, the cut along the section plane is performed, i.e. the normal strain ϵ_z as well as the shear strains γ_{xz} and γ_{yz} are set to zero at the plane. Finally, the displacement field induced by the stress field is computed which yields a simulated fresh cut with nodges as shown in Fig. 6.

Using the method, it is possible to compare the true histogram φ of the sphere radii with that one estimated by Eq. (4) from the simulated imprints. As Fig. 7 shows, the estimated and true φ are approximately the same. The root-mean-square deviation between the φ_k(true) and the φ_k(est) is 0.5%. The small shift of φ to lower values is mainly a consequence of the discretization of the integral equation (1). A smaller spacing Δ would reduce this systematic error, but in case of a low number of observed nodges, a small Δ will increase the statistical error of the estimated φ.

Tomography

From the rubber R1, an additional sample was studied in order to investigate the filler dispersion by µCT. Fig. 8 shows a volume rendering of the 3D sub-image, where the filler appears opaque, and the rubber matrix is transparent. The effective size of the corresponding µCT image was $715 \times 650 \times 845$ µm^3. Because of the high contrast between filler and rubber matrix, the particles can be segmented by simple binarization (using a constant threshold level) followed by a labelling of connected components with respect to the 26-adjacency of the pixels. The total number of filler particles in the image was about 46 900. From each of the particles, the size (i.e. the mean width over 13 space directions) and the volume v were determined, where

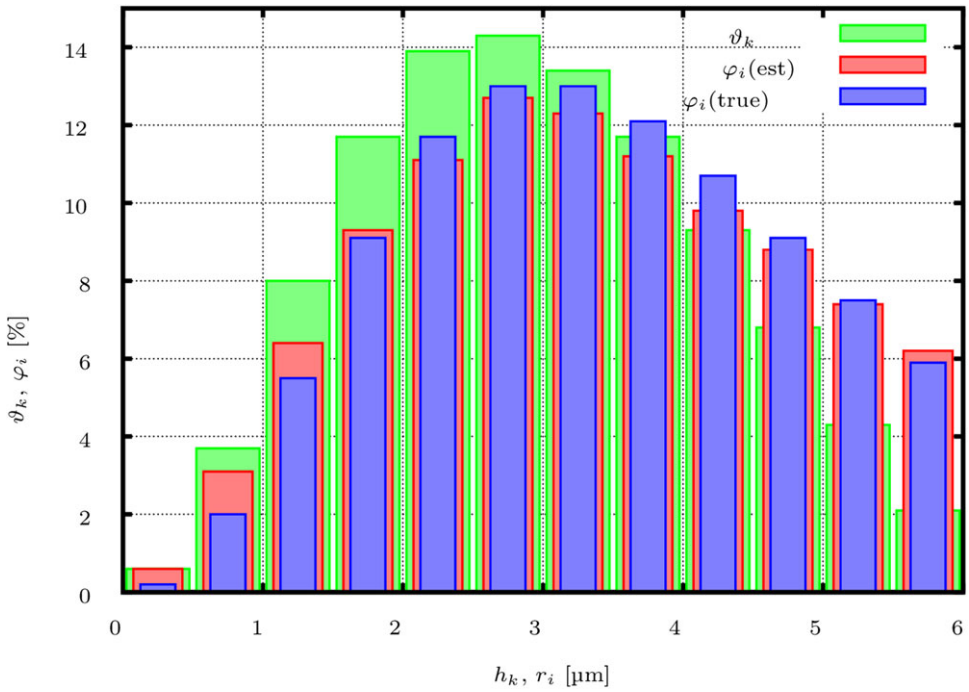

Fig. 7. Histograms ϑ and φ of volume-weighted distributions of nodge height respectively, filler particle size, bin width of 0.5 µm: The true φ known from the generation of the sphere system is compared with the estimated φ obtained by Eq. (4) from the histogram ϑ of the volume-weighted height distribution of simulated imprints.

the half mean width is used as the radius of the adapted sphere. For details on 3D image processing and analysis (in particular on the choice of pixel adjacency); see Ohser & Schladitz (2009). The volume fraction of particles with size larger than 2 µm was 0.06%. That means that the degree of dispersion is about 100%.

In Fig. 5A, the histogram of the volume-weighted particle size distribution estimated from the sub-volume shown in Fig. 8 is compared with that one stereologically estimated from the histogram of the volume-weighted height distribution of the nodges. The estimated relative frequencies of both histograms differ only slightly. The root-mean-square deviation between the φ_k(µCT) and the φ_k(est) is 0.4%. It turns out that image acquisition of fresh cuts of rubber specimens using the radiometric stereo microscope nSPEC 3D combined with a stereological estimation of the size distribution of the filler particles is an appropriate method for evaluation of macro-dispersion.

To justify the sphere assumption for the globular filler particles made in Section **Stereological Equation**, the shape factor

$$f_1 = 6\sqrt{\pi}\frac{V}{\sqrt{S^3}}$$

of a particle was determined from the 3D data, where V and S are the volume and the surface area of the particle, respectively; see Ohser & Schladitz (2009). This shape factor is normalized in such a way that $f_1 = 1$, if the particle is of

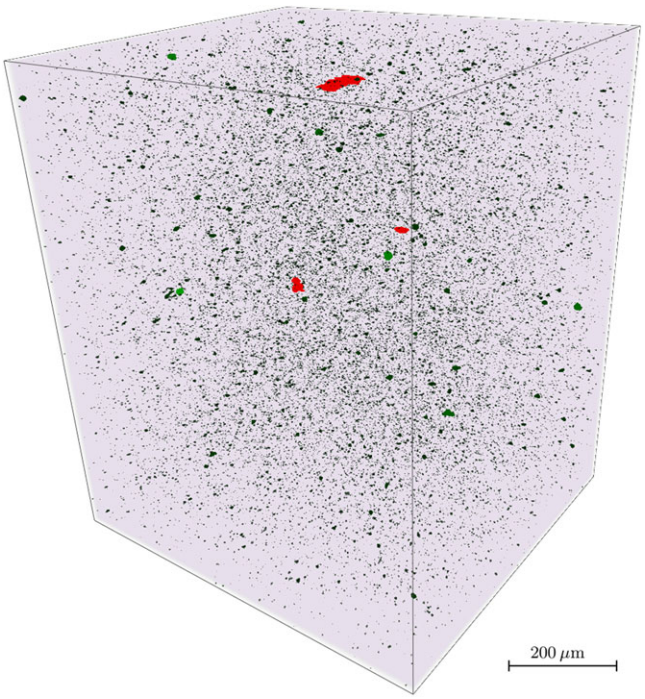

Fig. 8. Tomographic image showing carbon black filler particles in rubber: volume rendering of a sub-volume of 1100×1000×1300 pixels out of the complete 3D data set with 2560×2 560×2160 pixels of size 0.65 µm. Filler particles (or particle agglomerates) of a volume larger than 100 µm^3 are highlighted in red.

spherical shape. In cases of a non-spherical particles, one obtains values for f_1 between 0 and 1 describing various aspects of the deviation from sphere shape. The mean and standard deviation of this shape factor over all particles in the tomographic image shown in Fig. 8 are 0.986 and 0.041, respectively, i.e. the deviations from spherical shape are relatively small.

Discussion and conclusion

RSM presents a practical method of accurately estimating the volume-weighted size distribution of the filler particles (nodges) in rubber samples (fresh cuts) by allowing for the direct determination of the surface topology. The uneven contours of this 3D surface are a representation of the size and distribution of the nodges. The height of each bump, relative to the median surface, corresponds to the radii of the spherical nodges. A spherical model is assumed for all nodges due to the expected geometry of carbon black and the utilization of established stereological principles to accurately predict the total distribution of filler in the entire formulation.

We remark that the volume of the nodges considerably differs from that of the sphere caps. On the other hand, the nodges are only slightly higher than the ball caps. The reason for that is that a thin layer of the rubber matrix encloses the top of the caps. The unknown difference Δh between the heights of nodges and caps is the layer thickness. This difference implies a small shift of the estimated histograms of the particle size distribution to the right (i. e. to higher values). In our approach, the difference between the heights of nodges and caps was ignored (set to zero). On the other hand, the difference Δs between the size s_1 of white spots (observed by DFM) and the true size s_2 of the section profiles of the particles is much larger than Δh. Thus, the shift of the histogram of the estimated area-weighted size distribution of the white spots can be considerable. Even more dramatic are the effects on the estimation of the volume fraction V_V of the filler particles and, thus, on the degree of dispersion: While the area fraction A_A of the section profiles is equivalent to the volume fraction V_V of the particles, the area fraction of the white spots can be dramatically larger than V_V. This generally leads to a significant overestimation of the volume fraction URF of the unresolved filler from DFM images.

Basically, one could fit a model to the nodges, where a suitable model is, e.g. the Gaussian function

$$g_\sigma(x) = he^{-\frac{\|x\|^2}{2\sigma^2}}, \qquad x \in \mathbb{R}^2$$

with $\sigma = \sqrt{rh/2}$. This Gaussian is centred at the orthogonal projection of the particle centre on the section plane, and the principal curvatures of $g_\sigma(x)$ at $x = 0$ are the same as that of the ball cap. Then the volume v of the nodges is $v(r, h) = \pi r h^2$. This is very close to the approach used in Section **Stereological Equation** and would lead to similar results of the stereological estimation of the volume weighted particle size distribution.

In this work, we have shown by a simulation study that the particle size distribution stereologically estimated from simulated fresh cuts is largely consistent with the true particle size distribution used as input of this study. Furthermore, we did supplementary investigations by μCT using synchrotron radiation. The particle size distribution estimated from the tomographic data is nearly the same as the size distribution stereologically estimated from the data obtained by RSM.

The new microscopic method combined with the stereological estimation of size distribution presented in Section **Estimation of Particle Size Distribution** can be extended also on systems of non-spherically shaped polymeric particles (see Champion *et al.*, 2007), and other hydrocarbon polymers, which can be made of known irregular shape and dispersed in various media. Organic applications can include: histology (e.g. cell counting), hematology (e.g. analysis of biconcave red blood cells) and biomaterial (e.g. coating applications for tissue growth or adhesion).

The presented work is gauged against ASTM D7723–18 (2018) and ISO standards that provide guidelines on various classes of methods of quantifying filler percentage in rubber samples (electrical, mechanical, optical and miscellaneous) but stop short of describing a singular gold standard. This lack of a clear method presents an opportunity for new methods to overcome the limitation of current techniques and those previously adapted. Optical methods offer several advantages over other techniques, namely speed of measurement, system cost, automation, sample size, measurement accuracy and preserving the sample. Compared to μCT with synchrotron radiation, optical methods can be applied in parallel to active mixing processes, with minimal sample preparation, relatively low-cost and outside of specialized synchrotron light source facilities.

One of the most popular optical methods implemented in the dark field microscope is `DisperGRADER`, which utilizes a calibration reference standard of reflections to indirectly determine the filler amount in the dispersion. The presented work overcomes the need for a reference standard and the distortion (special and stereological) that arise from the use of reflections for a direct measure. Laser-based methods (laser profilometry and laser scanning) overcome some of these challenges but are not ideal for environments of rapid changes in topology (steep gradients) and noisy surfaces such as those of roughly cut rubber samples.

In contrast to shape from focus, radiometric stereo does not succumb to the problem of spatial oversampling in the z-axis. RSM also offers speed advantages (acquisition and computation) and a robustness of operation that makes it practical for deployment on an active production line. The system also

utilizes the same footprint as a conventional microscope (and common inspection systems), it does not require additional camera equipment, exotic external lighting or full encapsulation of the sample (e.g. cover of the sample from light), allowing for the use of minimal profile quick-attach sample holders. In contrast to other surface measures, radiometric stereo does not prevent the serial acquisition of reflected microscopy data, which is advantageous in case where the nodges exhibit fluorescent or other light properties that can aid in the stereological reconstruction of the surface volume. Radiometric stereo can also be used in conjunction with principles of structure from motion to provide additional information as a function of applied special changes in the sample. This is valuable in cases where a punch is used to obtain samples from the rubber or where the sample is quite large and cannot fit on a traditional holder. RSM is ideally suited for *in situ* applications as the system is mobile and can be placed on a moving track above the sample for rapid spatial scanning.

In conclusion, RSM offers a low-cost and practical method of acquisition images from fresh cuts surfaces of rubber specimens and stereological size distribution estimation of globular filler particles in a rubber matrix. In future work, we will further improve the quality of stereological estimation by replacing the numerical solution of Eq. (1) using the simple rectangular quadrature rule applied to Eq. (2) by the quasi-likelihood approach by Baaske *et al.* (2018), which allows the use of a parametric models for the particle size distribution. Furthermore, the assumption of a modified non-Lambertian reflectance, e.g. based on the solution of an explicit partial differential equation using Lax-Friedrich's sweeping method (see Ahmed & Farag, 2006) could improve the quality of image acquisition; see also Vogel *et al.* (2008) for an alternative approach related to Phong's reflection model. Finally, neuronal networks offer the advantage of training a model versus a known standard obtained by other techniques, such as atomic force microscopy. This training could increase the sensitivity for small nodges (small exposed height) and artefacts introduced by fresh cuts of rubber samples.

The new RSM allows a very accurate determination of the macro-dispersion of filler in rubber that meets the increasing requirements of industrial quality control. The measurement accuracy is superior to that of the DFM, since the particle size distribution can be determined directly with the RSM, while based on the DFM measurements only indirectly can be concluded on macro-dispersion, and even this indirect method can cause large errors. The cost of RSM and the measurement times are significantly higher than those of DFM. Nevertheless, they are on a scale appropriate for use in industrial laboratories. Finally, we remark that quality control with μCT has been established for a long time. However, high contrast imaging of carbon black in a rubber matrix requires (partially) coherent illumination combined with phase-retrieval, but until now this is only limited available for laboratory μCT.

Acknowledgements

This work was supported by the German Federal Ministry of Education and Research (BMBF) under grant 05M13RCA. The authors thank Dominik Etling from the University of Applied Sciences (Darmstadt) for fresh cut measurements performed with the `nSPEC 3D`. We thank the reviewers for their helpful comments.

References

Ahmed, A.H. & Farag, A.A. (2006) A new formulation for shape from shading for non-Lambertian surfaces. In *2006 IEEE Computer Society Conference on Computer Vision and Pattern Recognition (CVPR'06)*, vol. **2**, pp. 1817–1824. IEEE Press, Piscataway, NJ

Angulo, J. (2011) Morphological bilateral filtering and spatially-variant adaptive structuring functions. *Mathematical Morphology and its Applications to Image and Signal Processing, Proc. 10th International Symposium ISMM 2011, Verbania-Intra, Italy*, (ed. by P. Soille, M. Pesaresi & G.K. Ouzounis), volume LNCS **6671**, pp. 212–222. Springer, New York.

Arecchi, A.V., Messadi, T. & Koshel, R.J. (2007) *Field Guide to Illumination*. SPIE Press, Washington, DC.

ASTM D3053–17a (2017) *Standard Terminology Relating to Carbon Black*. ASTM, West Conshohocken, PA.

ASTM D663–14 (2014) *Standard Methods for Carbon Black-Dispersion in Rubber*. ASTM, West Conshohocken, PA.

ASTM D7723–18 (2018) *Standard Test Method for Rubber Property – Macro-Dispersion of Fillers in Compounds*. ASTM, West Conshohocken, PA.

Baaske, M., Ballani, F. & Illgen, A. (2018) On the estimation of parameters of a spheroid distribution from planar sections. *Spatial Statist.* **26**, 83–100.

Bathe, K.-J. (1996) *Finite Element Procedures in Engineering Analysis*. Prentice Hall, London.

Beucher, S. & Meyer, F. (1993) The morphological approach to segmentation: the watershed transform. *Mathematical Morphology in Image Processing*, (ed. by E. Dougherty), pp. 433–481. Marcel Dekker, New York.

Champion, J.A., Katare, Y.K. & Mitragotri, S. (2007) Making polymeric micro- and nanoparticles of complex shapes. *Proc. Nat. Acad. Sci. U.S.A.* **29**, 11901–11904.

Chen, L., Yang, Z. & Sun, L. (2008) Fast autofocus of microscopy images based on depth-from-defocus. In *IEEE RSJ International Conference on Intelligent Robots and Systems*, 22–26 Sept. 2008, Nice, France, pp. 3115–3120. IEEE Press, Piscataway, NJ.

Chiu, S.N., Stoyan, D., Kendall, W.S. & Mecke, J. (2013) *Stochastic Geometry and its Application*, 3rd edn. Wiley, Chichester.

Clark, D. & Brown, B. (2015) A rapid image acquisition method for focus stacking in microscopy. *Microsc. Today*. **23**(4), 18–24.

Cloetens, P., Barrett, R., Baruchel, J., Guigay, J.-P. & Schlenker, M. (1996) Phase objects in synchrotron radiation hard X-ray imaging. *J. Phys. D: Appl. Phys.* **29**(1), 133–146.

Douissard, P.-A., Cecilia, A., Rochet, X., Chapel, X., Martin, T., van de Kamp, T., Helfen, L., T., B., Luquot, L., Xiao, X., Meinhardt, J. & Rack, A. (2012) A versatile indirect detector design for hard X-ray microimaging. *J. Instrum.* **7**(9), P09016.

Frankot, R.T. & Chellappa, R. (1990) Estimation of surface topography from SAR imagery using shape from shading techniques. *Art. Intell.* **43**, 271–310.

Hess, W.M. & Chrico, V.E. (1977) Elastomer blend properties – influence of carbon black type and location. *Rubber Chem. Technol.* **50**, 301–326.

Le, H.H., Ilisch, S., Kasaliwal, G.R. & Radusch, H.-J. (2008) Filler phase distribution in rubber blends characterised by thermographic analysis of the rubber-filler gel. *Chem. Technol.* **81**, 767–782.

Miché, P., Bensrhair, A. & Leburn, D. (2005) Passive 3D shape recovery of unknown objects using cooperative polarimetric and radiometric stereo vision processes. *Opt. Eng.* **44**, 027005.

Mirone, A., Brun, E., Gouillart, E., Tafforeau, P. & Kieffer, J. (2014) The PyHST2 hybrid distributed code for high speed tomographic reconstruction with iterative reconstruction and a priori knowledge capabilities. *Nucl. Instrum. Meth. Phys. Res. B* **324**, 41–48. 1st International Conference on Tomography of Materials and Structures.

Ohser, J. & Mücklich, F. (2000) *Statistical Analysis of Microstructures in Materials Science*. Wiley, Chichester.

Ohser, J. & Nagel, W. (1988) On the stereological estimation of weighted sphere diameter distributions. *Acta Stereol.* **7**, 17–31.

Ohser, J. & Sandau, K. (2000) Considerations about the estimation of the size distribution in Wicksell's corpuscle problem. In editors, *Statistical Physics and Spatial Statistics. Lecture Notes in Physics*, vol. **554**, (ed. by K. Mecke & D. Stoyan), pp. 185–202. Springer, Berlin.

Ohser, J. & Schladitz, K. (2009) *3D Images of Materials Structures – Processing and Analysis*. Wiley-VCH, Weinheim.

Otsu, N. (1979) A threshold selection method from gray-level histograms. *IEEE Trans. Syst. Man. Cybernet.* **9**, 62–66.

Paganin, D., Mayo, S.C., Gureyev, T.E., Miller, P.R. & Wilkins, S.W. (2002) Simultaneous phase and amplitude extraction from a single defocused image of a homogeneous object. *J. Microsc.* **206**, 33–40.

Rack, A., Weitkamp, T., Riotte, M. *et al.* (2010) Comparative study of multilayers used in monochromators for synchrotron-based coherent hard X-ray imaging. *J. Synchrotron Radiat.* **17**(4), 496–510.

Ray, R., Birk, J. & Kelley, R.B. (1983) Error analysis of surface normals determined by radiometry. *IEEE Trans. Pattern Anal. Machine Intell.*, PAMI-5, pp. 631–645.

Soille, P. (1999) *Morphological Image Analysis*. Springer-Verlag, Berlin.

Vogel, O., Breuß, M. & Weickert, J. (2008) Perspective shape from shading with non-Lambertian reflectance. In Rigoll, G., editor, *Pattern Recognition* (ed. by G. Rigoll), pp. 517–526. Springer, Berlin.

Wang, M.-J. (2005) New development in carbon black dispersion. *Elastomers Plast.* **58**, 626–637.

Weitkamp, T., Haas, D., Wegrzynek, D. & Rack, A. (2011) *ANKAphase*: software for single-distance phase retrieval from inline X-ray phase-contrast radiographs. *J. Synchrotron Radiat.* **18**(4), 617–629.

Weitkamp, T., Tafforeau, P., Boller, E. *et al.* (2010) Status and evolution of the ESRF beamline ID19. *AIP Conf. Proc.* **1221**, 33–38.

Wicksell, S.D. (1925) The corpuscle problem I. *Biometrika* **17**, 84–89.

Wicksell, S.D. (1926) The corpuscle problem II. *Biometrika* **18**, 152–172.

Woodham, R.J. (1974) Gradient and curvature from the photometric-stereo method, including local confidence estimation. *J. Opt. Soc. Am. A* **11**, 3050–3068.

Woodham, R.J. (1980) Photometric method for determining surface orientation from multiple images. *Opt. Eng.* **19**, 139–144.

Zhang, R., Tsai, P.-S., E., C.J. & Shah, M. (1999) Shape-from-shading: a survey. *IEEE Trans. Pattern Anal. Machine Intell.* **21**, 690–706.

Zienkiewicz, O. C., Taylor, R. L. & Zhu, J. Z. (2005) *Finite Element Method: Its Basis and Fundamentals*, 6th ed. Elsevier, Amsterdam.